Projection onto the Manifold of Elongated Structures for Accurate Extraction

Amos Sironi[1]* Vincent Lepetit[1,2] Pascal Fua[1]
[1]CVLab, EPFL, Lausanne, Switzerland, {firstname.lastname}@epfl.ch
[2]TU Graz, Graz, Austria, lepetit@icg.tugraz.at

Abstract

Detection of elongated structures in 2D images and 3D image stacks is a critical prerequisite in many applications and Machine Learning-based approaches have recently been shown to deliver superior performance. However, these methods essentially classify individual locations and do not explicitly model the strong relationship that exists between neighboring ones. As a result, isolated erroneous responses, discontinuities, and topological errors are present in the resulting score maps.

We solve this problem by projecting patches of the score map to their nearest neighbors in a set of ground truth training patches. Our algorithm induces global spatial consistency on the classifier score map and returns results that are provably geometrically consistent. We apply our algorithm to challenging datasets in four different domains and show that it compares favorably to state-of-the-art methods.

1. Introduction

Reliably extracting boundaries from images is a long-standing open Computer Vision problem and finding 3D membranes, their equivalent in biomedical image stacks, while difficult is often a prerequisite to their segmentation. Similarly in both regular images and image stacks, reconstructing the centerline of linear structures is a critical first step in many applications, ranging from road delineation in 2D aerial images to modeling neurites and blood vessels in 3D biomedical image stacks.

These problems are all similar in that they involve finding elongated structures of codimension 1 or 2 given very noisy data. In all these cases, classification- and regression-based approaches [9, 38, 39] have recently proved to yield better performance than those that rely on hand-designed filters. This success is attributable to the representations used by powerful machine learning techniques [23, 43] operating on large training datasets.

However, these methods essentially classify individual pixels or voxels and do not explicitly model the strong relationship that exists between neighboring ones. As a result, isolated erroneous responses, discontinuities, and topological errors are not uncommon in the resulting score maps they produce, as illustrated by Fig. 1. Up to a point, these problems can be mitigated by using Auto-context like techniques [43], as in [40], or relying on structured learning to model correlations between neighbors, as in [12].

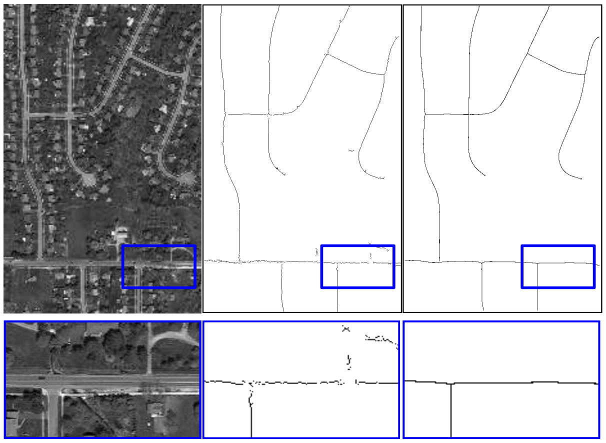
(a) Image (b) [40] (c) Ours

Figure 1. Pixel-wise classifiers reach state-of-the-art performance in several computer vision tasks. However, the response of such methods does not take into account the very particular structure and the spatial relation present in the ground truth images. (a) An aerial road image. For this problem the ground truth is composed by a continuous 1-D curve. (b) Output of a state-of-the-art method [40]. Since this method is based on pixel-wise regression, its output presents discontinuities on the centerlines and isolated responses on the background. (c) The output of our method is obtained by projecting the patches of the score image of (b) into the closest ground truth patches from the training images. In this way the structure of the ground truth patches is transferred to the score image, resulting in a provably correct global spatial structure.

In this paper, we show that an even better way is to first compute a score map using an appropriately trained regressor and then systematically replace pixel neighborhoods by their nearest neighbors in a set of ground truth training patches.

*This work was supported in part by the EU ERC project MicroNano.

This is in the spirit of algorithms for image denoising and inpainting that search for nearest neighbors within the image itself [11, 10, 25]. It is also closely related to the approach of [16] that improves boundary images by finding nearest neighbors using a distance defined in terms of descriptors extracted by a Convolutional Neural Network. By contrast, in our method, we compute distances in terms of the patches themselves and we will show that it improves both performance, especially near junctions, and generality.

In short, our algorithm induces global spatial consistency on the classifier score map and improves classification performance, as can be seen in Fig. 1(c). Furthermore, assuming that the structure of all admissible ground truth images is well represented by the set of training patches, it can be formally shown that our method is equivalent to projecting the score map into the manifold of all admissible ground truth maps.

2. Related Work

In this section, we review related work on centerline, boundary and membrane detection.

Centerline Detection Centerline detection methods can be divided in two main classes.

The first class relies on hand-designed filters. They are typically used to compute the Hessian matrix [14, 36, 28, 13, 29] or the Oriented Flux matrix [22, 1, 41, 33, 44], whose eigenvalues then serve to estimate the likelihood that a pixel or voxel lies on a centerline. Since the filters are optimized for ideal tubular structure, their performance decreases when the structures of interest become irregular.

To overcome this limitation, a second class of methods that rely on Machine Learning techniques has recently emerged. Classification-based ones [17, 47, 7, 46] have been successfully applied to the segmentation of thick linear structures while, regression-based ones [39, 40] have been shown to be particularly effective at finding centerline pixels only. However, even if pixel-wise classification and regression methods can produce remarkable results, they do not explicitly model the strong relationship that exists between neighboring pixels. As a consequence, discontinuities and inconsistencies may occur in their output.

Boundary Detection Boundary detection methods can be divided in the same two classes as for centerline detection.

All the early approaches [26, 8, 32] belong to the first one and rely on filters designed to respond to specific image intensity profiles. Recently, attention has shifted to classification based methods [5, 34, 38, 24, 12], which have produced significant improvements.

More specifically, in [5] gradients on different image channels are fed to a logistic regression classifier to predict contours. In [34], SVMs are trained to predict boundaries from features computed using sparse coding. In [9], a Deep Convolutional Network is used to segment cell membranes in 2D Electron Microscopy slices, while a sequence of classifiers is used in [38] for boundary detection in both natural images and Electron Microscopy data.

However, as in the case of centerline detection, none of these methods explicitly model the relationship between nearby pixels. In particular, the response of Convolutional Neural Networks [23] can be spatially inconsistent because they typically treat every pixel location independently, thus relying only on the fact that neighboring patches share pixels to enforce consistency.

By contrast, in Auto-context based methods [43, 38], features extracted from the classifiers output in earlier layers enlarge the receptive field and often yield more spatially consistence results. However, these methods are prone to overfitting and require large amount of training data to prevent it. The method of [12] overcomes these problems by relying on structured learning, resulting in an accurate and extremely efficient edge detector. It is inspired by the work of [20, 21] where the structured random forest framework is introduced for image labeling purposes, predicting for every pixel an image patch, instead of single pixel probabilities. However, it is specific to the particular kind of classifier used for learning and is difficult to generalize.

Recently, Nearest Neighbors search in the space of local descriptors obtained with a Convolutional Network was used for boundary detection purposes [16]. Given an image patch, the algorithm computes a corresponding descriptor and then looks for the Nearest Neighbor in a dictionary built from the training set. While effective, this approach strongly depends on the specific dictionary learned by the CNN. Therefore, when it fails, it is difficult to understand why. Our method is closely related, but we perform Nearest Neighbors search in the space of the final output, rather than of intermediate image features. We will show empirically that it works better, especially near junctions. Moreover, unlike other approaches, ours is provably correct under certain conditions, thus giving insights and indications on how to improve the results.

Membrane Detection Membranes are the 3D equivalent of contours in image stacks. They are important for 3D volume segmentation, especially in a biomedical context [45, 4, 15]. In the previous paragraph we mentioned algorithms [9, 38] that extract them 2D slice by 2D slice. Here we discuss those that extract them as 3D surfaces.

As in the case of 2D boundaries, early approaches to detecting them relied on hand-crafted filters optimized to respond to ideal sheet-like structures. In [37, 30, 27] for example, the eigenvalues of the Hessian matrix are combined to obtain a score value that is maximal for voxels lying on a 2D surface. Similarly, the eigenvalues of the Oriented Flux matrix [22] can be combined to obtain a score that is less sensitive to adjacent structures.

More recent approaches have focused on machine learning techniques. For example, a Convolutional Neural Network and a hierarchical segmentation framework combining Random Forest classifier and watersheds are used in [19] and [3] respectively to segment neural membranes. Even though both of these methods produce excellent results, they are designed for tissue samples prepared with an extra-cellular die that highlights cell membranes while suppressing the intracellular structures, thus making the task comparatively easy.

3. Motivation and Formalization

As discussed in Section 2, methods that rely on statistical classification techniques currently deliver the best results for boundary, centerline, and membrane detection. Among those, it has recently been reported that regression-based ones perform best for centerline detection [39] and we will demonstrate here that they perform equally well for boundary and membrane detection.

More specifically, the algorithm of [39] involves training regressors to return distances to the closest centerline in scale-space. In this way, performing non-maximum suppression on their output yields both centerline locations and corresponding scales. This has proved very effective but, like for all other pixel-based techniques that do not incorporate any *a priori* geometric knowledge that may be available, this approach can easily result in topological mistakes.

In this paper, we first extend this approach to both boundary and membrane detection. We then demonstrate that we can correct the errors it makes by projecting them into the manifold of distance transforms corresponding to the kind of structures we are trying to reconstruct. This results in a technique that is both a more competent and more widely applicable method than the original one [39]. Furthermore, it is generic in the sense that it is applicable to other methods returning a score map, such as [12, 9].

In the remainder of this section, we first summarize the approach of [39] and show that it extends naturally to boundary and membrane detection. We also introduce the formalism that we will use in the next section to describe our approach to improving the distance transforms by projecting them onto an appropriate manifold.

3.1. Centerline Detection

Let $I \in \mathbb{R}^N$ be an image containing linear structures and let Y be the corresponding binary ground truth image, such that $Y(p) = 1$ if pixel p is on a centerline and $Y(p) = 0$ otherwise.

Finding the centerlines can be formulated as the pixel classification problem of learning a mapping between a feature vector $f_M(p, I)$, extracted from a local neighborhood $\mathcal{N}_M(p)$ of size M around pixel p in image I, and the value $Y(p)$.

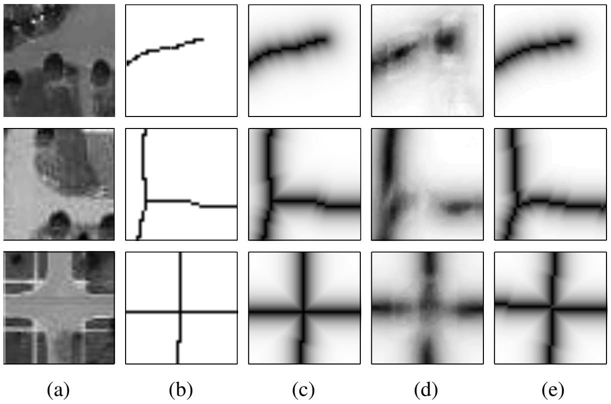

Figure 2. Centerline Detection as a Regression Problem. (a) Original image patch; (b) Centerlines Ground Truth; (c) Distance Function of Eq. (1) proposed in [39]; (d) The response of a pixel-wise regressor trained to predict the function in (c) is discontinuous and returns topologically incorrect results, also when Auto-context [43] is applied. (e) Nearest Neighbors of the score patches in (d), found in the training set. In our method we apply Nearest Neighbors search to a regressor output and take advantage of the particular structure of ground truth patches to correct its mistakes.

Learning such a classifier, however, can be difficult in practice because of the similar aspect of nearby pixels to the centerline and ambiguities on the exact location of a centerline due to low resolution and blurring.

To address this difficulty, the method of [39] replaces the binary ground truth Y by the modified distance transform of Y

$$d(p) = \begin{cases} e^{a(1-\frac{\mathcal{D}_Y(p)}{d_M})} - 1 & \text{if } \mathcal{D}_Y(p) < d_M \\ 0 & \text{otherwise} \end{cases}, \qquad (1)$$

where $\mathcal{D}_Y$ is the Euclidean distance transform of Y, $a > 0$ is a constant that controls the exponential decrease rate of d close to the centerline and d_M a threshold value determining how far from a centerline d is set to zero.

Function d has a sharp maximum along the centerlines and decreases as one moves further from them. Fig. 2(c) shows examples of function d computed on small patches. Learning a regressor to associate the feature vector $f_M(p, I)$ to $d(p)$ induces a unique local maximum in the neighborhood of the centerlines. This approach is more robust to small displacements and returns centerlines that are better localized compared to classification-based methods.

To learn the regressor we apply the GradientBoost algorithm [18]. Given training data $\{f_i, d_i\}_i$, where $f_i = f_M(p_i, I)$ is the feature vector corresponding to pixel p_i and $d_i = d(p_i)$, GradientBoost learns a function $\varphi(\cdot)$ of the form $\varphi(q) = \sum_{t=1}^{T} \alpha_t h_t(q)$, where $q = f_M(p, I)$ denotes a feature vector, h_t are weak learners and $\alpha_t \in \mathbb{R}$ are weights. Function φ is built iteratively, selecting one weak learner and its weight at each iteration, to minimize a loss function $\mathcal{L}$ of the form $\mathcal{L} = \sum_i L(d_i, \varphi(f_i))$.

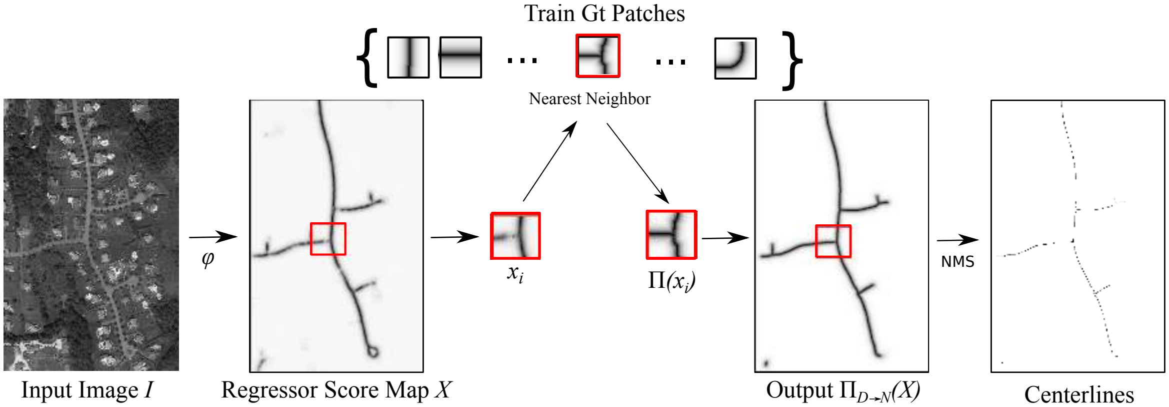

Figure 3. Method overview. A score map X is obtained from image I by applying a regressor φ trained to return distances from the centerlines. Every patch x_i of size D in X is projected onto the set of ground truth training patches, by nearest neigbor search. The projected patches $\Pi_N(x_i)$ are averaged to form the output score map $\Pi_{D\to N}(X)$. Centerlines are obtained by Non-Maxima Suppression.

In addition, to learn the best possible regressor, we adopted the Auto-context technique [43], as in [40] and using the same parameters. To this end, we use the score map $\varphi(\cdot)$ to extract a new set of features that are added to the original ones to train a new regressor.

3.2. Boundary and Membrane Detection

The method described above extends naturally to boundary detection. As centerlines, boundary in 2D images and membranes in 3D image stacks are elongated structures of codimension 1 and there are substantial ambiguities in the exact boundary location.

Therefore, and as before, we replace the binary ground truth, provided for such problems, by the distance transform of Eq. (1). The distance function is computed 2D for boundaries and 3D for membranes. We then train a regressor to associate feature vectors to the distances to the boundaries. We can obtain the boundaries from the score map returned by the regressor by non-maxima suppression.

4. Improving the Distance Function

The central element of our approach is to project the distance transform produced by pixel-wise regression, as described in the previous section, onto the manifold of all possible ones for the structures of interest. Since this manifold is much too large to be computed in practice, we first propose a practical computational scheme and then formally prove that it provides a close approximation under assumptions that can be made to hold in the real world.

4.1. Nearest Neighbors Projections

Given an image I and corresponding binary ground truth Y, let dY be the image obtained by applying function d of Eq. (1) to every pixel of Y. Since it corresponds to pixels belonging to specific structures, Y is constrained to have well defined geometric properties. For example, in the case of centerlines or boundaries in images, Y is composed of 1-dimensional curves, while for boundaries in 3D volumes, Y is a 2D surface. This means that the set of all admissible ground truths forms a manifold in the set of binary images. Similarly, the set of images dY forms a manifold in the set of real valued images, which we will denote by $\mathcal{M}_N$.

Let X be the score map obtained by applying the regressor φ to each pixel of an input image I. Ideally we would like X to be an element of $\mathcal{M}_N$, so that it is guaranteed to be geometrically correct. However, this is not true in general. Fig. 2(d) shows typical errors committed at critical points, such as T-junctions. This is a standard problem with many edge detectors, such as the Canny detector.

In theory, one way to avoid this problem is to project X into $\mathcal{M}_N$, which is equivalent to finding the element of $\mathcal{M}_N$ closest to X,

$$\Pi_N(X) = \operatorname*{arg\,min}_{dY \in \mathcal{M}_N} \|dY - X\|^2. \tag{2}$$

In practice, however, $\mathcal{M}_N$ is not known or much too large to be sampled exhaustively. Therefore, $\Pi_N(X)$ can not be computed directly.

As shown in Fig. 3, our solution is to approximate it by projecting small patches of X onto the set of ground truth train patches.

Formally, let $\mathcal{M}_D = \{y_k\}_{k=1}^K$ be the set of training patches of size D, extracted form local neighborhoods $\mathcal{N}_D$ in the ground truth training images. For each pixel p_i, $i = 1, \ldots, N$ in the score image X, let $x_i = X(\mathcal{N}_D(p_i))$ be the squared neighborhood of size D around p_i.

For every i, we consider the projection of x_i into $\mathcal{M}_D$, given by

$$\Pi_D(x_i) = \operatorname*{arg\,min}_{y \in \mathcal{M}_D} \|y - x_i\|^2. \tag{3}$$

Fig. 2(d) shows examples of nearest neighbors for three score patches. We then average all these projections to obtain a new score image $\Pi_{D\to N}(X)$.

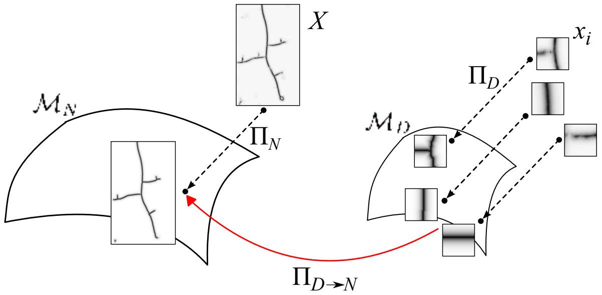

Figure 4. The output $\Pi_{D\to N}(X)$ of our method can be seen as projection of the score map X into the manifold of admissible ground truth images $\mathcal{M}_N$. This is achieved by projecting small patches x_i of X into the set of ground truth patches $\mathcal{M}_D$ and then averaging the resuls to obtain $\Pi_{D\to N}(X)$.

More precisely, given the set of projected patches $\{\Pi_D(x_i)\}_{i=1}^N$, we take the pixel values of the new image $\Pi_{D\to N}(X)$ to be

$$\Pi_{D\to N}(X)(p) = \frac{1}{R} \sum_{i:p-p_i \in \mathcal{N}_R(p)} \Pi_D(x_i)(p-p_i), \quad (4)$$

where $R \leq D$ is the size of the neighborhood used for averaging and where we take $\Pi_D(x_i)$ to be centered at zero, with $\Pi_D(x_i)(p-p_i)$ the value of $\Pi_D(x_i)$ at $p-p_i$.

The image $\Pi_{D\to N}(X)$ obtained in this way is an approximation of $\Pi_N(X)$. In the next section, we introduce sufficient conditions under which $\Pi_N(X) = \Pi_{D\to N}(X)$ and we provide a formal proof in the supplementary material.

4.2. Equivalence of $\Pi_{D\to N}(X)$ and $\Pi_N(X)$

In this section we state under which conditions the output $\Pi_{D\to N}(X)$ of our method is equivalent to the projection $\Pi_N(X)$ of the score image X into the manifold of all admissible ground truth images $\mathcal{M}_N$. The two necessary properties are:

(i) The training set of patches $\mathcal{M}_D$ is composed of all admissible ground truth patches and averaging patches of $\mathcal{M}_D$ that coincide for overlapping pixels, gives an image of $\mathcal{M}_N$;

(ii) For two patches x_i and x_j, extracted from overlapping neighborhoods $\mathcal{N}_D(p_i)$ and $\mathcal{N}_D(p_j)$ in image X, their projections $\Pi_D(x_i)$ and $\Pi_D(x_j)$ coincide for all pixels in the intersection of $\mathcal{N}_D(p_i) \cap \mathcal{N}_D(p_j)$.

We formalize these concepts in the supplementary material, where we also prove that under these conditions our method amounts to project the score map X into the ground truth manifold $\mathcal{M}_N$. Fig. 4 illustrates this equivalence. Intuitively, this means that the output of our method is the best approximation of X, in the space of ground truth images. Therefore, it also has the same geometrical properties.

In practice, these conditions will never be strictly satisfied. However, we also show in the supplementary material that by relaxing them and assuming only approximated projections, we can prove that the error we make is within a given bound to the optimal solution. This bound can be estimated from the error committed by the projections on the patches $\Pi_D(x_i)$ and the size of our training set compared to the set all admissible training patches.

5. Results

To demonstrate the versatility of our method, we evaluate it on four very different problems, road centerline detection in aerial images, blood vessels delineation in retinal scans, membrane detection in 3D Electron Microscopy (EM) stacks and boundary detection in natural images. The code used in our experiments is available online.

5.1. Centerline Detection

We use a publicly available dataset of grayscale aerial images [1] such as the one of Fig. 1, in which we aim at finding the road centerlines. This dataset comprises 13 training- and 13 test-images. For each one, manually annotated road centerlines and widths are available. We used this training data to learn the regressor of Section 3.1, for which the code is available online [1]. To compute the score maps we use as input, we embedded the regressor in an Auto-Context [43] framework, as suggested in [40] to improve the regressor output. As can be seen in Fig. 1(b), the result while state-of-the-art can still be improved, especially near junctions, which is illustrated in Fig. 1(c).

To this end, we used the approach of Section 4.1 with patch sizes $D = 81 \times 81$ and $R = 21 \times 21$. To build the training set of patches used in the nearest neighbor search, we randomly sampled $3 \cdot 10^5$ patches from locations within a distance of 16 pixels to the ground truth centerlines to which we added a uniform patch of zeros, corresponding to the background. We also randomly rotated the training patches to obtain a more general dataset. For Nearest Neighbor search we use the FLANN library [31]. Moreover, we take advantage of the sparsity of the ground truth images to reduce the computational cost. It is easy to show that if the maximum of a score patch x_i is smaller than a given threshold, its nearest neighbor is necessary the uniform patch of zeros. In this way we can avoid calculating the nearest neighbor for up to 50% of pixels. More details are given in the supplementary material. In our Matlab implementation, processing a small 620 × 505 image on a multi-core machine took a few seconds and a larger 1185 × 898 one about 40.

For this dataset, we found that the use of a large patch size D is required to correct the mistakes of the regressor. However, using a too large value for D makes it difficult to gather a representative training set of patches. As a consequence, a large value for D can result in loss of details.

[1] http://cvlab.epfl.ch/software/centerline-detection.

Table 1. Aerial dataset results. The values correspond to the F-measure computed on whole image (first row) and on pixels close to junctions only (second row). Our method is more accurate than the state-of-the-art, in particular close to junctions.

	SE [12]	**Reg-AC** [40]	**Reg-AC-NLM**	**Reg-AC-KSVD**	**Ours SingleScale**	**Ours MultiScale**
Whole image	0.93	0.91	0.93	0.93	0.94	**0.95**
Junctions only	0.89	0.82	0.87	0.87	0.92	**0.94**

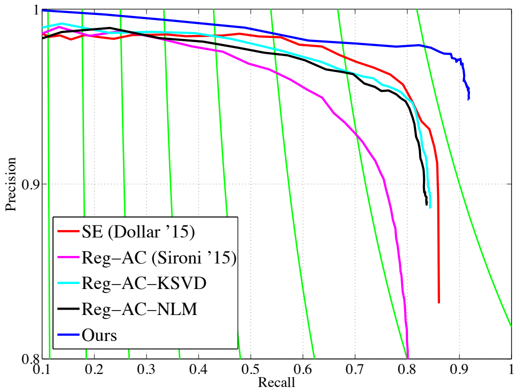

Figure 5. Precision-Recall curves for junction accuracy on Aerial dataset. See the text for a description of the different methods. Our method outperforms the baselines by a large margin and it is more accurate than applying standard denoising schemes to the score map. Best viewed in color.

To handle this trade off, we adopted a multi-scale approach. Instead of considering directly patches of size D for nearest neighbor search, we concatenate their central parts of size D' and their downsampled version to size D' together into a single vector, and we perform nearest neighbor search on the resulting vectors. We then use the patch of size D' corresponding to the nearest vector to build the projection. In practice, we use $D = 81 \times 81$ and $D' = 41 \times 41$.

We will refer to our approach as **Ours-SingleScale** and **Ours-Multiscale** depending on whether we use this multi-scale approach or not.

Baselines We consider the algorithm we used to produce our input score maps [40] and the Structured Edge detector of [12], which we will refer to as **Reg-AC** and **SE** respectively. For the latter, we used the code provided by [12] and trained a structured Random Forest to predict the centerline locations. To highlight the importance of using ground truth images for nearest neighbor search, we also applied Non-Local Means denoising, which relies on nearest neighbor search of patches in image itself, to the score images we used as input for our algorithm. We also applied to them K-SVD denoising [2], where the required dictionary was built from the ground truth images. We used the code provided by the authors of [35, 2]. We experimented with different parameters and found consistently similar results. We will refer to these approaches as **Reg-AC-NLM** and **Reg-AC-KSVD**, respectively.

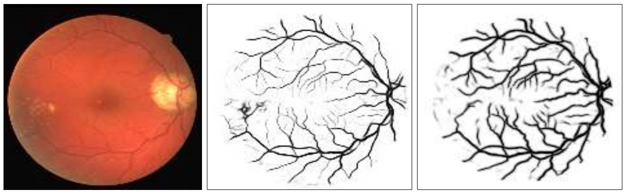

(a) (b) (c)

Figure 6. DRIVE dataset results. (a) Image; (b) **N^4-Fields** [16]; (c) **Ours**. Our method responds strongly on thin vessels and is less sensitive to the bright structured noise on the left part of the image.

Evaluation We applied non-maxima suppression to the output of all methods to find the actual centerlines and used the evaluation procedure of the Berkeley benchmark [5]. We computed Precision-Recall curves that include a tolerance factor for centerline localization. In Table 1, we give the results for a 2 pixel tolerance and those for different values in the supplementary material. The rankings are mostly independent of the choice of this factor and our approach comes out consistently ahead.

This evaluation does not account for the topological properties of the centerlines. Therefore, since junctions are present only at sparse image locations, errors close to junctions have only a small influence on the final performance. This is a weakness of this evaluation scheme because accurate delineation near junctions is particularly important for subsequent processing steps. To remedy this, we recomputed the Berkeley metrics only near junctions. More precisely, we automatically identified from the test ground truth images the junction locations and then considered 21×21 regions centered around them. We then computed the Precision-Recall curves only there. The Precision-Recall curves for a tolerance of 2 pixels are shown in Fig. 5 and the corresponding F-measures given in Table 1. Note that the advantages of our method and in particular the multi-scale approach are even more marked near junctions, where ambiguities are strongest.

5.2. Vessel Segmentation

We consider the problem of segmenting blood vessels in retinal scans. To test our approach we consider the DRIVE dataset [42], which comprises 20 training images and 20 test images of size 565×584.

We train a regressor to return distances from the blood vessels. For this task, the structure of interest, while still elongated, is not limited to centerlines and has a visible

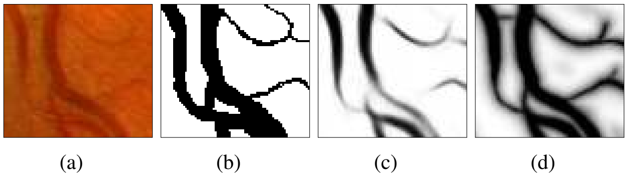

Figure 7. Vessel Segmentation. Raw image and score maps on a region with complex topology. (a) Image; (b) Ground truth; (c) **N^4-Fields**; (d) Our approach. Our method recovers jucntions in the image even in regions with very low contrast and for very thin structures.

width. Therefore, we trained the regressor to return its maximal response over the whole width of the blood vessels, instead of only at centerlines as for Section 5.1. We then applied nearest neighbor projection with patch sizes of Section 4.1 equal to $D = 13 \times 13$ and $R = 7 \times 7$. We sampled all training patches within a distance of 6 pixels to a vessel and randomly rotating them.

We compare our approach with **SE** [12], **N^4-Fields** [16] and **KernelBoost** [7]. Table 2 shows the F-measure obtained with the different methods. Our approach is comparable or better than the state-of-the-art [7] and [16].

To study the behavior of the methods close to junctions, which are of great importance to get the topology of the vessels right, but have little influence on the performance computed on the whole image, we repeated the junctions evaluation, similarly to Section 5.1. As shown in Table 2 our method outperforms the baselines by a large margin. Fig. 6 shows the results on a test image. Fig. 7 shows the results on a particularly complex region of a test image, with several thin junctions and low contrast. Our method can correctly reconstruct the topology of the blood network, which [16] fails to achieve. Moreover, as can be seen from Fig. 7, our method is more accurate than the ground truth in some part of the images. This actually penalizes our method when evaluating on the whole image.

Table 2. DRIVE results. The table shows the F-measure for the different methods computed on the whole image and only on regions around a junction. Our method reaches state-of-the art performance on the dataset and outperforms the other methods on the junction evaluation.

	Whole image	Junctions only
SE [12]	0.67	0.52
Reg-AC [40]	0.79	0.71
KernelBoost [7]	0.80	0.76
N^4-Fields [16]	**0.81**	0.74
Ours	**0.81**	**0.80**

5.3. Membrane Segmentation

In this section we consider the problem of membrane detection in 3D EM stacks. Our dataset is made of four stacks of size $250 \times 250 \times 309$. The first stack is used for training, the second for validation, and the last two for testing. An expert annotated all voxels belonging to dendrites in these volumes. From these, we automatically extracted the dendritic boundary voxels that form the the membranes. Since other cells such as axons and ganglions are also present but not annotated, we only considered the voxels within a distance of 11 voxels from the dendrites for both training and evaluation.

The Context Cue Features of [6] have proved to very effective for EM supervoxel classification and we use them here as input to the regressor of Section 3.2.

We applied our method to the output score returned by the regressor after 0, 1, and 2 Auto-context iterations. For this task smaller patches gave better results, so we used patch sizes $D = 9 \times 9$ and averaging on a $R = 5 \times 5$ window. We sampled $2 \cdot 10^6$ truth patches within a distance of 6 pixels to a vessel plus a uniform patch of zeros, for nearest neighbor search. For comparison purposes, we also applied Non-Local Means denoising to the score maps. All the parameters were optimized using the validation volume. Processing a test stack took about 6 minutes.

As for the centerlines, to account for potential inaccuracies in the annotations, we compute the performance with different tolerance factors. The F-measures for a tolerance of 3 voxels are shown in Table 4. The values for other tolerance factors and the Precision-Recall curves are given in the supplementary material and the rankings are similar.

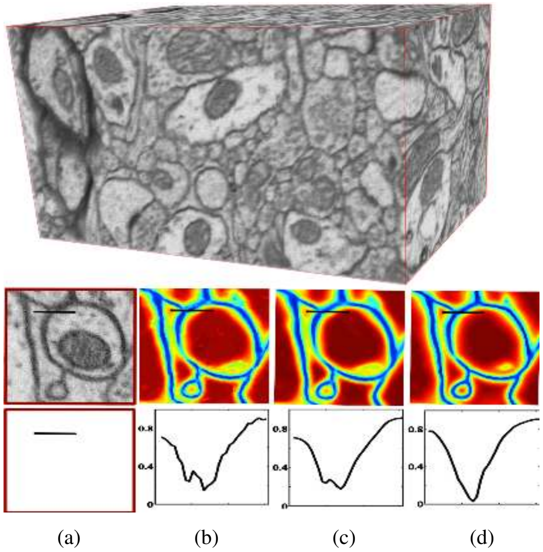

Figure 9. Top row: A test stack used in in our experiments. Middle row: Detail of a slice of a test stack and responses of different methods. (a) Image; (b) Initial score map. (c) Non-Local Means applied to (b). (d) Our approach applied to (b). Bottom row: intensity values along the orizontal black lines in the images. Our method removes background spurious responses while sharpening the response on the membranes. The smoothing effect of the Non-Local Means approach instead decreases accuracy on the junctions. Best viewed in color.

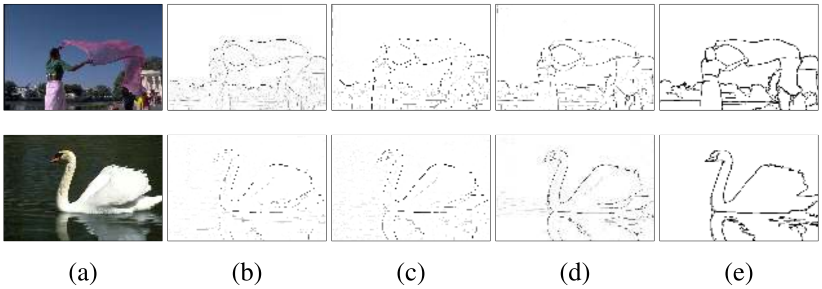

Figure 8. Boundary Detection Results. (a-e) Boundaries obtained by non-maxima suppression on the score image returned by different methods. (a) Image; (b) **SE** [12]; (c) **N^4-Fields** [16] (d) **Ours**; (e) Human annotation. Our approach returns more continuous boundaries and preserves important details, like for example the right hand of the lady on the top image and the beak of the swan in the bottom image.

Table 3. BSDS dataset results.

	ODS	OIS	AP
SCG [34]	0.74	0.76	0.77
SE [12]	0.74	0.76	**0.80**
N^4-Fields [16]	0.75	0.77	0.78
Ours	**0.76**	**0.78**	0.76

Our approach always brings an improvement compared to the baseline. Applying Non-Local Means to the score map made the performance slightly worse in this case. This is probably because applying Non-Local Means smoothes the regressor's response while our approach keeps it sharp, especially close to junctions, as shown in Fig. 9.

Table 4. F-measure for the Membrane Detection dataset. We applied our approach to the output of [6], trained to predict the regression function of Section 3.1, at different Auto-context iterations. Notice that our method applied at the first Auto-context iteration performs better ($F = 0.87$) than the other methods at the second iteration ($F = 0.85$ and $F = 0.84$).

	No AC	AC iter 1	AC iter 2
ContextCues [6]	0.78	0.84	0.85
ContextCues + NLM	0.76	0.83	0.84
Ours	**0.81**	**0.87**	**0.88**

5.4. Boundary Detection

To test our method on the boundary detection task, we consider the BSDS benckmark dataset [5]. The dataset is composed of 200 training, 100 validation and 200 test images of size 481×321 pixels.

We trained our regressor with the same parameters as in Section 5.1. We ran our approach with patch size $D = 21\times21$ and $R = 11\times11$ sampling $3\cdot10^6$ train patches. As is done [34, 12, 16], we ran our detector on the test images at 3 different resolutions—half, original, and double size—and then averaged the results. Finally, non-maxima suppression was applied to the score map for evaluation purposes.

Table 5.2 shows an improvement for the ODS and OIS scores compared to the state-of-the-art. The corresponding curves are shown in the suplementary material. Fig. 8 depicts the boundaries detected by the different methods on two test images. Processing one image at the three different scales took less than one minute.

6. Conclusion

We have proposed an effective method to detect centerlines, segment linear structures, and find boundaries and membranes.

We have shown that it compares favorably to the state-of-the-art and can be understood as an efficient projection onto the manifold of feasible solutions. This means that domain knowledge, such as engineering constraints on roads and biological ones on blood vessels and membranes, could be introduced as a preprocessing step by refining this manifold. In practice, this could mean cleaning-up the patches we sample from it, which we will investigate in future work.

Acknowledgments We thank Bohumil Maco for his meticulous work in annotating the EM dataset.

References

[1] G. Agam and C. Wu. Probabilistic Modeling-Based Vessel Enhancement in Thoracic CT Scans. In *CVPR*, 2005.

[2] M. Aharon, M. Elad, and A. Bruckstein. K-SVD: An Algorithm for Designing Overcomplete Dictionaries for Sparse Representation. *Trans. Sig. Proc.*, 2006.

[3] B. Andres, U. Koethe, M. Helmstaedter, W. Denk, and F. Hamprecht. Segmentation of SBFSEM Volume Data of Neural Tissue by Hierarchical Classification. In *DAGM*, pages 142–152, 2008.

[4] B. Andres, T. Kröger, K. L. Briggman, W. Denk, N. Korogod, G. Knott, U. Köthe, and F. A. Hamprecht. Globally Optimal Closed-Surface Segmentation for Connectomics. *ECCV*, 2012.

[5] P. Arbelaez, M. Maire, C. Fowlkes, and J. Malik. Contour Detection and Hierarchical Image Segmentation. *PAMI*, 33(5):898–916, 2011.

[6] C. Becker, K. Ali, G. Knott, and P. Fua. Learning Context Cues for Synapse Segmentation. *TMI*, 2013.

[7] C. Becker, R. Rigamonti, V. Lepetit, and P. Fua. Supervised Feature Learning for Curvilinear Structure Segmentation. In *MICCAI*, September 2013.

[8] J. Canny. A Computational Approach to Edge Detection. *PAMI*, 8(6), 1986.

[9] D. Cireşan, A. Giusti, L. Gambardella, and J. Schmidhuber. Deep Neural Networks Segment Neuronal Membranes in Electron Microscopy Images. In *NIPS*, 2012.

[10] A. Criminisi, P. Perez, and K. Toyama. Region Filling and Object Removal by Exemplar-Based Image Inpainting. *TIP*, 2004.

[11] K. Dabov, A. Foi, and V. Katkovnik. Image Denoising by Sparse 3D Transformation-Domain Collaborative Filtering. *JMLR*, 16(8):1–16, August 2007.

[12] P. Dollár and C. L. Zitnick. Fast Edge Detection Using Structured Forests. *PAMI*, 2015.

[13] A. H. Foruzan, R. A. Zoroofi, Y. Sato, and M. Hori. A Hessian-Based Filter for Vascular Segmentation of Noisy Hepatic CT Scans. *International Journal of Computer Assisted Radiology and Surgery*, 7(2):199–205, 2012.

[14] A. Frangi, W. Niessen, K. Vincken, and M. Viergever. Multiscale Vessel Enhancement Filtering. *Lecture Notes in Computer Science*, 1496:130–137, 1998.

[15] J. Funke, D. Andres, F. A. Hamprecht, A. Cardona, and M. Cook. Efficient Automatic 3D-Reconstruction of Branching Neurons from EM Data. *CVPR*, 2012.

[16] Y. Ganin and V. Lempitsky. n^4-Fields: Neural Network Nearest Neighbor Fields for Image Transforms. In *ACCV*, 2014.

[17] G. Gonzalez, F. Aguet, F. Fleuret, M. Unser, and P. Fua. Steerable Features for Statistical 3D Dendrite Detection. In *MICCAI*, pages 625–32, September 2009.

[18] T. Hastie, R. Tibshirani, and J. Friedman. *The Elements of Statistical Learning*. Springer, 2001.

[19] V. Jain, J. Murray, F. Roth, S. Turaga, V. Zhigulin, K. Briggman, M. Helmstaedter, W. Denk, and H. Seung. Supervised Learning of Image Restoration with Convolutional Networks. In *ICCV*, pages 1–8, 2007.

[20] P. Kontschieder, S. Bulo, H. Bischof, and M. Pelillo. Structured Class-Labels in Random Forests for Semantic Image Labelling. In *ICCV*, 2011.

[21] P. Kontschieder, S. R. Bulò, M. Donoser, M. Pelillo, and H. Bischof. Semantic Image Labelling as a Label Puzzle Game. In *BMVC*, 2011.

[22] M. Law and A. Chung. Three Dimensional Curvilinear Structure Detection Using Optimally Oriented Flux. In *ECCV*, 2008.

[23] Y. LeCun, L. Bottou, Y. Bengio, and P. Haffner. Gradient-Based Learning Applied to Document Recognition. *PIEEE*, 1998.

[24] J. Lim, C. L. Zitnick, and P. Dollár. Sketch Tokens: A Learned Mid-Level Representation for Contour and Object Detection. In *CVPR*, 2013.

[25] J. Mairal, F. Bach, J. Ponce, G. Sapiro, and A. Zisserman. Non-Local Sparse Models for Image Restoration. In *ICCV*, 2009.

[26] D. Marr and E. Hildreth. Theory of Edge Detection. *Proceedings of the Royal Society of London, Biological Sciences*, 207(1167):187–217, 1980.

[27] A. Martinez-Sanchez, I. Garcia, and J. Fernandez. A Ridge-Based Framework for Segmentation of 3D Electron Microscopy Datasets. *Journal of Structural Biology*, 2013.

[28] E. Meijering, M. Jacob, J.-C. F. Sarria, P. Steiner, H. Hirling, and M. Unser. Design and Validation of a Tool for Neurite Tracing and Analysis in Fluorescence Microscopy Images. *Cytometry Part A*, 58A(2):167–176, April 2004.

[29] H. Mirzaalian, T. Lee, and G. Hamarneh. Hair Enhancement in Dermoscopic Images Using Dual-Channel Quaternion Tubularness Filters and MRF-Based Multi-Label Optimization. *TIP*, 2014.

[30] K. Mosaliganti, F. Janoos, A. Gelas, R. Noche, N. Obholzer, R. Machiraju, and S. Megason. Anisotropic Plate Diffusion Filtering for Detection of Cell Membranes in 3D Microscopy Images. In *ICBI*, 2010.

[31] M. Muja and D. G. Lowe. Scalable Nearest Neighbor Algorithms for High Dimensional Data. *PAMI*, 2014.

[32] W. Neuenschwander, P. Fua, G. Székely, and O. Kubler. Initializing Snakes. In *CVPR*, pages 613–615, June 1994.

[33] M. Pechaud, G. Peyré, and R. Keriven. Extraction of Tubular Structures over an Orientation Domain. In *CVPR*, 2009.

[34] X. Ren and L. Bo. Discriminatively Trained Sparse Code Gradients for Contour Detection. In *NIPS*, December 2012.

[35] J. Salmon and Y. Strozecki. Patch Reprojections for Non Local Methods. *Signal Processing*, 2012.

[36] A. Santamaría-Pang, T. Bildea, C. M. Colbert, P. Saggau, and I. Kakadiaris. Towards Segmentation of Irregular Tubular Structures in 3D Confocal Microscope Images. In *MICCAI Workshop in Microscopic Image Analysis and Applications in Biology*, 2006.

[37] Y. Sato, C.-F. Westin, A. Bhalerao, S. Nakajima, N. Shiraga, S. Tamura, and R. Kikinis. Tissue Classification Based on 3D Local Intensity Structure for Volume Rendering. *IEEE Trans. on Visualization and Computer Graphics*, 2000.

[38] M. Seyedhosseini, M. Sajjadi, and T. Tasdizen. Image Segmentation with Cascaded Hierarchical Models and Logistic Disjunctive Normal Networks. In *ICCV*, 2013.

[39] A. Sironi, V. Lepetit, and P. Fua. Multiscale Centerline Detection by Learning a Scale-Space Distance Transform. In *CVPR*, 2014.

[40] A. Sironi, E. Turetken, V. Lepetit, and P. Fua. Multiscale Centerline Detection. *PAMI*, 2015.

[41] M. Sofka and C. Stewart. Retinal Vessel Centerline Extraction Using Multiscale Matched Filters, Confidence and Edge Measures. *TMI*, 2006.

[42] J. Staal, M. Abramoff, M. Niemeijer, M. Viergever, and B. van Ginneken. Ridge Based Vessel Segmentation in Color Images of the Retina. *TMI*, 2004.

[43] Z. Tu and X. Bai. Auto-Context and Its Applications to High-Level Vision Tasks and 3D Brain Image Segmentation. *PAMI*, 2009.

[44] E. Turetken, C. Becker, P. Glowacki, F. Benmansour, and P. Fua. Detecting Irregular Curvilinear Structures in Gray Scale and Color Imagery Using Multi-Directional Oriented Flux. In *ICCV*, December 2013.

[45] A. Vazquez-Reina, M. Gelbart, D. Huang, J. Lichtman, E. Miller, and H. Pfister. Segmentation Fusion for Connectomics. In *ICCV*, 2011.

[46] J. D. Wegner, J. A. Montoya-Zegarra, and K. Schindler. A Higher-Order CRF Model for Road Network Extraction. In *CVPR*, 2013.

[47] Y. Zheng, M. Loziczonek, B. Georgescu, S. Zhou, F. Vega-Higuera, and D. Comaniciu. Machine Learning Based Vesselness Measurement for Coronary Artery Segmentation in Cardiac CT Volumes. *SPIE*, 7962(1):79621–7962112, 2011.